Supplementary Materials

Tailoring Polarization Homogeneity in Discontinuous-Columnar $Bi(Fe,Mn)O_3$ Thin Films through Strain Engineering via Controlled Dislocation Self-Assembly

Huiting Sui[1], Wenhua Lou[1], Shibing Xiao[4], Jia He[3], Fuling Wu[3], Ying Liu[1], Jianbiao Wei[1], Haijie Lu[1], Huajun Sun[3,*], Xiaoguang Ma[1,*], Shujun Zhang[2,*]

[1]School of Physics and Optoelectronic Engineering, Ludong University, Yantai, China.

[2]City University of Hong Kong.

[3]State Key Laboratory of Silicate Materials for Architectures, Wuhan University of Technology, Wuhan, China.

[4]College of Chemistry and Material Science, Hengyang Normal University, Hengyang, China.

Corresponding author. *E*-mail: huajunsun@whut.edu.cn; hsiaoguangma@ldu.edu.cn; s.j.zhang@cityu.edu.hk.

Phase-field Simulations of the Evolution of Polarization Behaviors

In the phase-field simulation, the ferroelectric polarization is simulated by solving the time-dependent (Ginzburg-Landau) (TDGL) equation for the temporal evolution of the polarization vector field[1,2]:

$$\frac{\partial P_i(r,t)}{\partial t} = -L\frac{\delta F}{\delta P_i(r,t)}, (i = 1,2,3) \quad (1)$$

where $P_i(r, t)$ is the polarization component, $r=(x_1, x_2, x_3)$ represents the spatial vector and t denotes time. L is a kinetic coefficient that is related to the domain mobility.

The total free energy F of the system comprises contributions from the Landau energy (f_{land}), gradient energy (f_{grad}), electric energy (f_{elec}), and elastic energy (f_{elas}), and is specifically described as follows:

$$F = \int_V (f_{land} + f_{grad} + f_{elec} + f_{elas})\, dV \quad (2)$$

The Landau energy f_{land} represents the bulk free energy density,

$$\begin{aligned} f_{land} = {} & \alpha_1(P_1^2 + P_2^2 + P_3^2) - \alpha_{11}(P_1^2 + P_2^2 + P_3^2)^2 + \alpha_{12}(P_1^2P_2^2 + P_2^2P_3^2 + P_3^2P_1^2) \\ & + \alpha_{112}(P_1^4P_2^2 + P_2^4P_3^2 + P_3^4P_1^2 + P_1^2P_2^4 + P_2^2P_3^4 + P_3^2P_1^4) \\ & + \alpha_{111}(P_1^2 + P_2^2 + P_3^2)^3 + \alpha_{123}(P_1^2P_2^2P_3^2) \end{aligned} \quad (3)$$

where P_1, P_2, P_3 are polarization components, α_{ij} are Landau energy coefficients. Among those coefficients, only α_1 depends on the temperature, which can be expressed by the Curie-Weiss law:

$$\alpha_1 = \frac{(T - T_C)}{2\varepsilon_0 C_0} \quad (4)$$

where T_c is the Curie temperature, C_0 is the Curie constant, and ε_0 is the permittivity of vacuum.

The gradient energy density can be expressed as:

$$f_{grad} = \frac{1}{2} g_{ijkl} P_{i,j} P_{k,l} \tag{5}$$

where g_{ijkl} is the gradient energy coefficient and $P_{i,j} = \frac{\partial P_i}{\partial x_j}$.

The electrostatic energy density f_{elec} of the system in phase-field simulation is composed of an external electric field and depolarization field.

$$f_{elec} = -\frac{1}{2} \varepsilon_0 \varepsilon_{ij} E_i E_j - E_i P_i \tag{6}$$

where ε_0 is the permittivity of vacuum and ε_{ij} is the background dielectric constant tensor.

The elastic energy density can be expressed as:

$$f_{elas} = \frac{1}{2} C_{ijkl} (\varepsilon_{ij} - \varepsilon_{ij}^0 - \varepsilon_{ij}^d)(\varepsilon_{kl} - \varepsilon_{kl}^0 - \varepsilon_{kl}^d) \tag{7}$$

where c_{ijkl} is the elastic stiffness tensor, ε_{ij} represents the total elastic strain, ${\varepsilon_{ij}}^0$ is the eigenstrain expressed as ${\varepsilon_{ij}}^0 = Q_{ijkl} P_k P_l$, $\varepsilon_{ij}^d = \Delta nx/u$ is the strain caused by dislocation, where Δnx_{ij}. represents a dislocation that produces n lattice spacings. The evolution of ferroelectric polarization was shown in Fig. 5g-h.

Tab. 1 Landau free energy coefficients for BFO at 25 °C[3]

Coefficients	BFO
α_1($C^{-2}\cdot m^2\cdot N$)	-3.73×10^8
α_{11}($C^{-4}\cdot m^6\cdot N$)	2.29×10^8
α_{12}($C^{-4}\cdot m^6\cdot N$)	3.064×10^8
α_{111}($C^{-6}\cdot m^{10}\cdot N$)	5.99×10^9
α_{112}($C^{-6}\cdot m^{10}\cdot N$)	-3.34×10^8
α_{123}($C^{-6}\cdot m^{10}\cdot N$)	-1.778×10^9

DFT Simulations

A 5×5×5 k-point mesh was adopted, with the electronic self-consistency convergence criterion set to 10^{-5} eV and the force convergence criterion set to 0.01 eV/Å to ensure thorough structural optimization. Additionally, standard pseudopotentials from the VASP library were selected for each element.

Modeling BFMO as Euler-Bernoulli Beam on a Winkler Foundation (Ni-Cr or LNO/Ni-Cr)

Boundary Conditions

I. At x = 0: Simply supported conditions

For a simply supported BFMO thin film at x = 0, the deflection and slope are constrained as follows:

$$\omega(0) = 0, \omega'(0) = 0 \tag{8}$$

These conditions represent the fact that the BFMO thin film is supported in such a way that it cannot translate or rotate at this end. Physically, the

deflection at the support point is zero ($\omega(0)=0$), and the slope ($\omega'(0)=0$) is constrained as the support prevents rotation.

II. At x= *L*: Applied Moment

At the point $x = L$, an external moment M is applied. The moment is related to the second derivative of the deflection through:

$$M = -EI\omega''(L) \tag{9}$$

This condition enforces the relationship between the applied moment and the curvature of the thin film at this location. The minus sign indicates the direction of the moment as per the BFMO thin films' curvature.

III. At x = *L*: Zero Shear Force

Additionally, it is assumed that the shear force at x = *L* is zero. Shear force is related to the third derivative of the deflection, and consequently:

$$\omega''''(L) = 0 \tag{10}$$

This condition arises naturally in cases where the BFMO thin film' end is free of transverse loads. Physically, it implies that no shear force acts at x = *L*, which is typical for cantilever-like conditions or free ends.

Stress Distribution

While solving *Eq*. (1) for ω(x), the stress distribution can be solved. The stress distribution ($\sigma(z)$) in *z*-direction is given by:

$$\sigma(z) = \sqrt{\sigma_f + \sigma_m(z)} \tag{11}$$

$$\sigma_f = \frac{k\omega}{S} \tag{12}$$

$$\sigma_m(z) = Ez\frac{d^2\omega}{dx^2} + \frac{N}{S} \tag{13}$$

where σ_f is the reaction stress of the foundation, σ_m is the stress from the bending moment (M) and axial force (N), $\sigma_m(z)$ represents the *z*-component of σ_m, and S is the area of the interface.

Analytical solution

I. Characteristic Equation

Assuming a solution of the form $\omega(\mathrm{x}) = e^{rx}$, substituting into the governing equation gives:

$$EIr^4e^{rx} + Nr^2e^{rx} + ke^{rx} = 0 \tag{14}$$

Dividing through by e^{rx} (non-zero), the characteristic equation can be obtained:

$$EIr^4 + Nr^2 + k = 0 \tag{15}$$

Setting $z = r^2$, then this becomes a quadratic equation in *z*:

$$EIz^4 + Nz^2 + k = 0 \tag{16}$$

Using the quadratic formula:

$$\mathrm{z} = \frac{-N \pm \sqrt{N^2 - 4EIk}}{2EI} \tag{17}$$

The roots of the characteristic equation are:

$$\mathrm{r} = \pm\sqrt{z} = \pm\sqrt{-N \pm \frac{\sqrt{N^2 - 4EIk}}{2EI}} \tag{18}$$

II. General Solution

The general solution of the differential equation depends on the nature of the roots:

①Distinct real roots: If $N^2 - 4EIK > 0$, there are four distinct real roots, and the general solution is:

$$\omega(\mathrm{x}) = C_1 e^{r_1 x} + C_2 e^{-r_1 x} + C_3 e^{r_2 x} + C_4 e^{-r_2 x} \tag{19}$$

where $r_1 = \sqrt{z_1},\ r_2 = \sqrt{z_2}$ are the roots of the characteristic equation.

② Complex roots: If $N^2 - 4EIK < 0$, the roots are complex, say $r = \alpha \pm i\beta$, and the general solution is:

$$\omega(\mathrm{x}) = e^{\alpha \mathrm{x}}\big(C_1 \cos(\beta \mathrm{x}) + C_1 \sin(\beta \mathrm{x})\big) + e^{-\alpha \mathrm{x}}\big(C_3 \cos(\beta \mathrm{x}) + C_4 \sin(\beta \mathrm{x})\big) \tag{20}$$

III. Applying Boundary Conditions

To determine the constants C_1, C_2, C_3, C_4, appropriate boundary conditions must be applied. These conditions depend on the physical constraints of the thin film and its supports. The boundary conditions collectively form a system of equations for the constants C_1, C_2, C_3, C_4. Substituting the general solution and its derivatives into these equations ensures the solution satisfies the physical constraints of the problem. Substituting the general solution and its derivatives into the boundary conditions forms a system of linear equations for C_1, C_2, C_3, C_4. Solving this system yields the specific solution ω(x).

Calculation of Polarization Vector

To analyze the positions and shapes of atomic columns in STEM images, we used ATOMAP, a free and open-source software tool based on 2D elliptical Gaussian fitting. The method involves iteratively fitting the most intense atomic columns, subtracting them from the image, and then extracting the positions of the remaining atoms. The BFMO thin film in this study exhibits an ABO_3 perovskite structure, with Bi occupying the larger A-site and Ti occupying the transition metal B-site.

The positions of all A-site and B-site atoms were determined through a three-step process: first, identifying the approximate locations of atomic columns; second, refining their positions via centroid optimization until convergence with a 2D Gaussian fit was achieved; and finally, fitting each column using a 2D elliptical Gaussian function $I(x, y)$, to precisely characterize their intensity distributions.

$$I(x, y) = I_0 + Aexp(-(a(x - x_0))^2 - 2b(x - x_0\big(y - y_0\big) + c(y - y_0)^2)) \tag{21}$$

$$a = \frac{cos^2\theta}{2\sigma_x^2} + \frac{six^2\theta}{2\sigma_y^2} \tag{22}$$

$$b = -\frac{sin2\theta}{4\sigma_x^2} + \frac{sin2\theta}{4\sigma_y^2} \quad (23)$$

$$c = \frac{sin^2\theta}{2\sigma_x^2} + \frac{cos^2\theta}{2\sigma_y^2} \quad (24)$$

where I_0 is the background, A is the amplitude, x_0 and y_0 are the center positions, σ_x and σ_y are the standard deviations, and θ is the rotation.

Following initial image filtering, the positions of A-site atoms were further refined using the original STEM image. The refinement process involved calculating the center of mass within a circular region (radius = 40% of the nearest A-site neighbor distance) centered at each provisional atomic position. These optimized coordinates served as initial parameters for fitting 2D Gaussian functions to all A-site atoms in the unprocessed STEM image.

Due to their higher intensity, A-site atoms dominated the image contrast. To enable robust fitting of the less intense B-site atoms, we first subtracted the fitted 2D Gaussian profiles of A-site atoms from the original image. This removal enhanced the relative contrast of B-site atoms, facilitating their precise localization using the same center-of-mass approach applied to A-site atoms.

All determined atomic positions (A-site and B-site) were cataloged separately for subsequent analysis. Using MATLAB, we processed the BFMO STEM images alongside the extracted atomic coordinates. For polarization analysis, each A-site atom was considered in the context of its four nearest B-site neighbors. Assuming these B-site atoms remained unaffected by polarization, their geometric center was calculated to represent the ideal, unperturbed A-site position. The displacement vectors between actual and ideal A-site positions were then computed, with arrow direction indicating polarization orientation and color gradient representing both magnitude and angular distribution of the displacements.

References

1. Höfling, M. et al. Control of polarization in bulk ferroelectrics by mechanical dislocation imprint. *Science* **372**, 961–964 (2021).
2. Yang, B.-B. et al. Engineering relaxors by entropy for high energy storage performance. *Nat Energy* **8**, 956–964 (2023).
3. Xu, S-Q. et al. Strain engineering of energy storage performance in relaxor ferroelectric thin film capacitors. *Adv. Theory Simul*. **5**, 2100324 (2022).

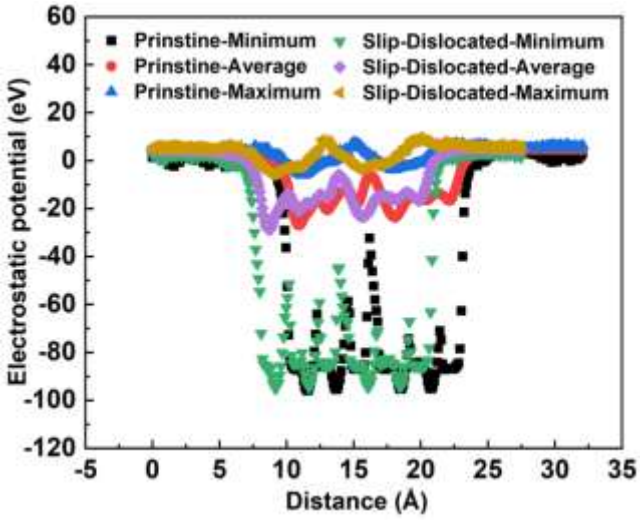

Fig. S1 The corresponding electrostatic potential distributions for the pristine BFMO and slip-dislocated BFMO samples.

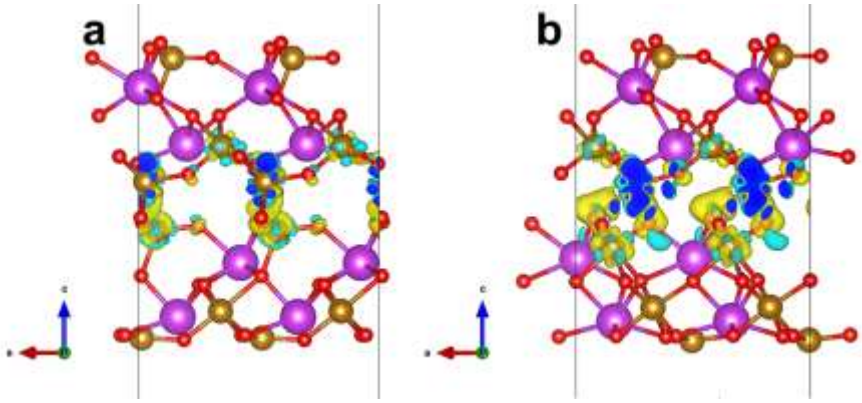

Fig. S2 Differential charge density of BFMO homojunction thin films, where yellow regions represent electron accumulation and blue regions indicate electron depletion. a Pristine structure with perfectly stacked BFMO layers, **b** slip-dislocated structure. The size of the isosurface is set to 0.008 e/Å^3.

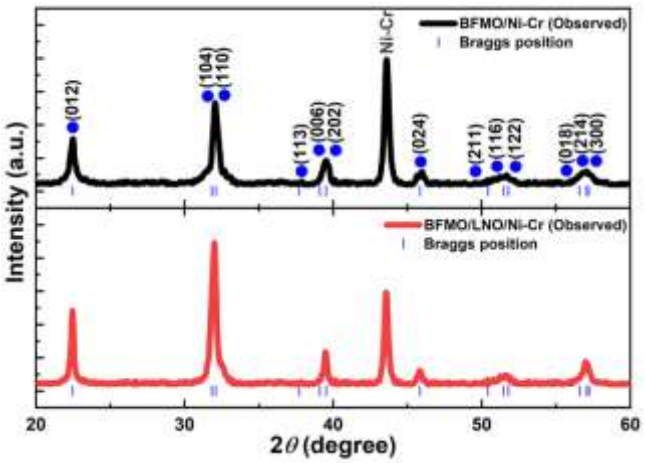

Fig. S3 XRD patterns of BFMO/Ni-Cr and BFMO/LNO/Ni-Cr in SAXS mode.

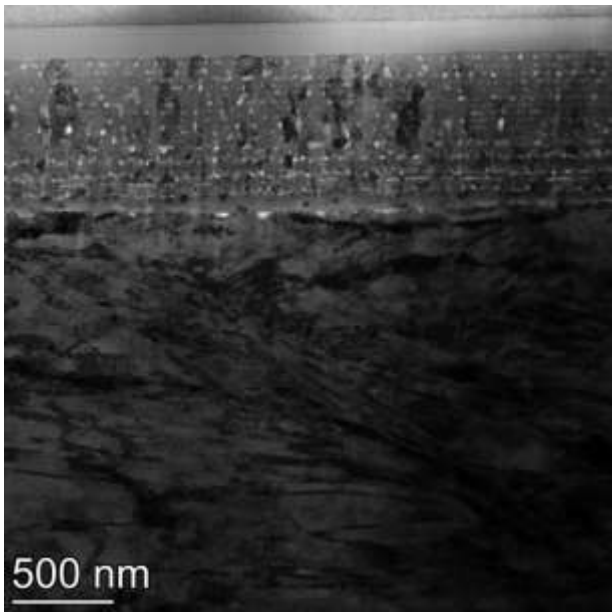

Fig. S4 The bright-field TEM micrograph of BFMO thin films on LNO/Ni-Cr with discontinuous columnar grains.

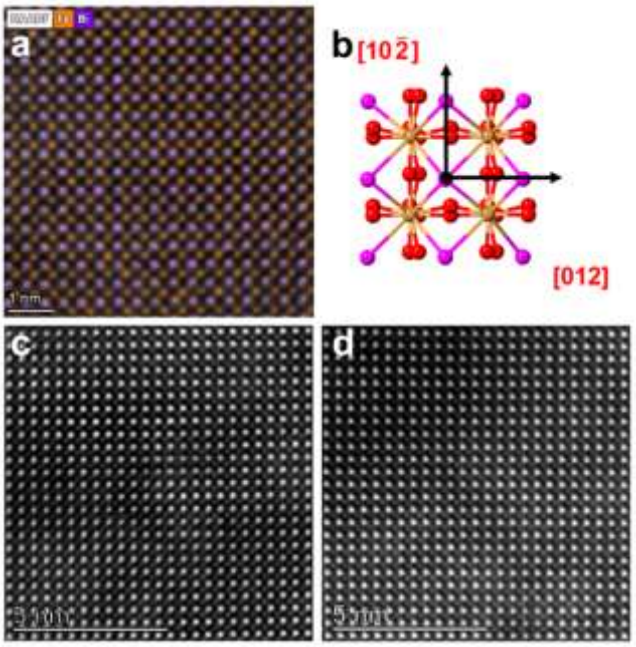

Fig. S5 HAADF-STEM images of BFMO thin films. a Element distribution of BFMO thin film on LNO/Ni-Cr, **b** FeO_6 octahedral structure of BFMO, **c** HADDF-STEM images corresponding to (a_1) in Fig. 4c, **d** HADDF-STEM images corresponding to (c_1) in Fig. 4c.

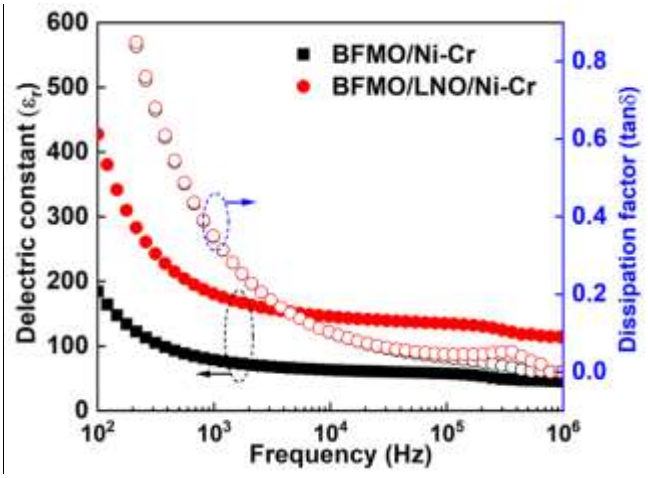

Fig. S6 Dielectric constant (ε_r) and dissipation factor (tanδ) versus frequency for BFMO thin films on Ni-Cr and LNO/Ni-Cr.

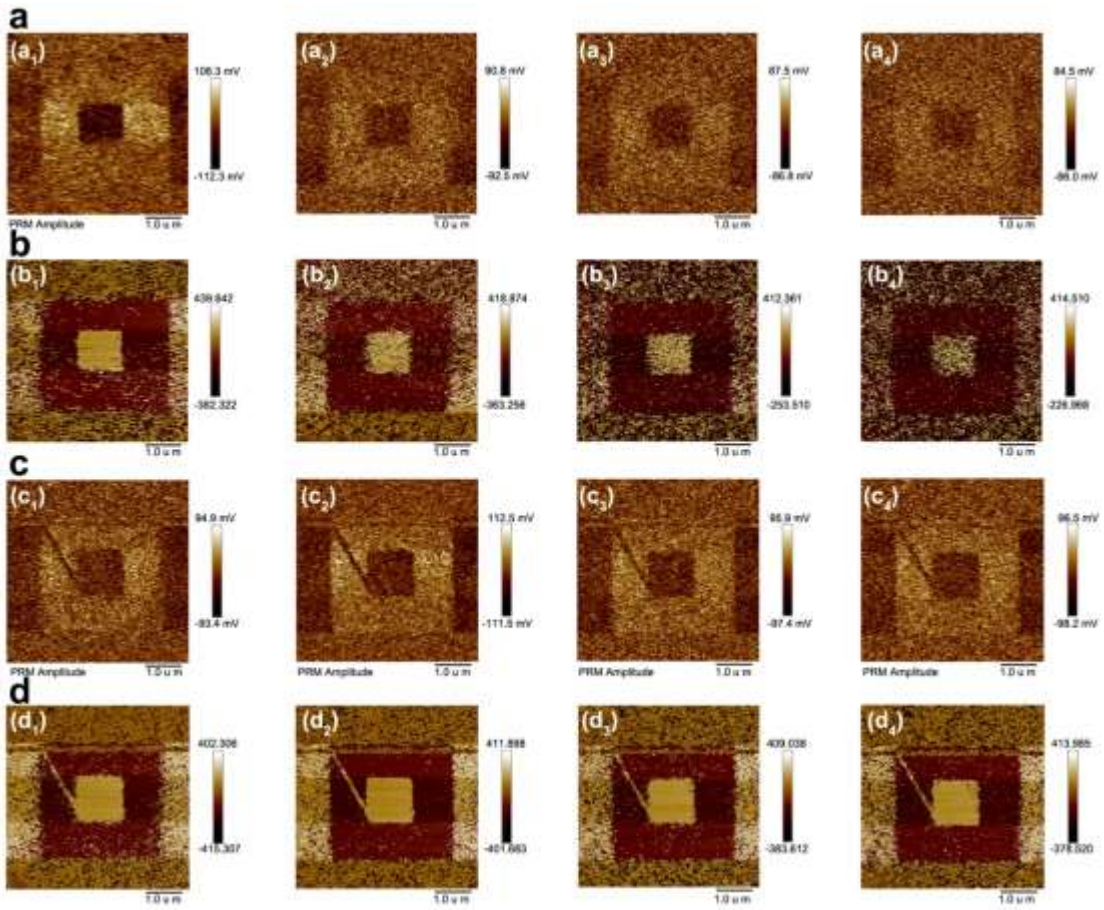

Fig. S7 Out-of plane PFM amplitude and phase images after poling treatment at ±10 V with relaxation durations of 0, 10 min, 20 min, 30 min and 40 min for BFMO on Ni-Cr and BFMO on LNO/Ni-Cr, respectively. $\mathbf{a_1}$-$\mathbf{a_5}$ amplitude images for BFMO on Ni-Cr, $\mathbf{b_1}$-$\mathbf{b_5}$ phase images for BFMO on Ni-Cr, $\mathbf{c_1}$-$\mathbf{c_5}$ amplitude images for BFMO on LNO/Ni-Cr, $\mathbf{d_1}$-$\mathbf{d_5}$ phase images for BFMO on LNO/Ni-Cr.